2023 7th International Conference on Computer Applications in Electrical Engineering-Recent Advances (CERA) | 979-8-3503-0500-5/23/$31.00 ©2023 IEEE | DOI: 10.1109/CERA59325.2023.10455370

Input Current FFT Model-derived Comprehensive Comparison of Totem-pole PFC and H-Bridge PFC Converter DM EMI Performances

Parth Rathod
Power Electronics and control Engineering Laboratory (PEACE)
Arizona State University
Mesa, USA
prathod3@asu.edu

Naveed Ishraq
Power Electronics and control Engineering Laboratory (PEACE)
Arizona State University
Mesa, USA
nishraq@asu.edu

Ashwin Chandwani
Power Electronics and control Engineering Laboratory (PEACE)
Arizona State University
Mesa, USA
avchandw@asu.edu

Ayan Mallik
Power Electronics and control Engineering Laboratory (PEACE)
Arizona State University
Mesa, USA
amallik3@asu.edu

***Abstract*— The paper describes the development of mathematical models for Totem-pole PFC (TPFC) and H-Bridge PFC (HPFC) and contrasts the results with simulation and experimental findings. An inner loop current controller and an outer loop voltage controller are both incorporated in the control system, which is accountable for ensuring a power factor close to unity and retains an output voltage of 400V DC. Using continuous Fast Fourier Transform (FFT) modeling, the work compares the input currents for both TPFC and HPFC converters. Total Harmonic Distortion (THD) was calculated to be contrasted with the simulated system and the experimental observations using the mathematically established input current waveshape. The design procedure for an EMI filter that will minimize differential mode (DM) noise and enhance front-end power quality is also covered in this paper. The implementation and evaluation of the 500-W TPFC and HPFC prototypes utilize 110V, 60Hz ac on the input side and deliver 400V dc at the output end with a switching frequency of 100kHz. The power factors for TPFC and HPFC are reported to be 0.983 and 0.989, respectively. The FCC class A EMI standard is met by the front-end DM EMI filter implementation, which provides the necessary attenuation.**

***Keywords*— Totem-pole PFC (TPFC), H-Bridge PFC (HPFC), Total Harmonic Distortion (THD), Continuous Conduction Mode (CCM), differential mode (DM), Electro-magnetic Interference (EMI), on-board battery charger (OBC)**

I. Introduction

Numerous viable techniques and topologies have emerged with the increasing growth of electric mobility and the electric vehicles (EVs) charging infrastructure [1]. Maintaining a power factor close to unity is essential in the utilization of Onboard Battery Chargers (OBC) in Electric Vehicles to enhance the power quality of the grid. Fig. 1 shows the typical circuit architecture of an EV OBC, for which, various PFC topologies have been discussed in [2]-[4]. Usually, the OBC is composed of two stages: a preliminary AC/DC converter and a subsequent isolated DC/DC converter. The two most common PFC topologies, TPFC and HPFC, which are easy to implement and are capable of sustaining high operating efficiency, are the main subjects of this work. The circuit schematics of TPFC and HPFC converters are shown in Fig. 2 comprising of four transistors. References [5] and [6] provide the better understanding about the modes of operation of TPFC and HPFC converters.

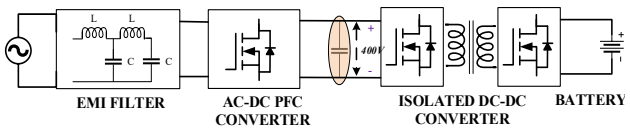

Fig. 1 An electrical block diagram of the onboard batter charger

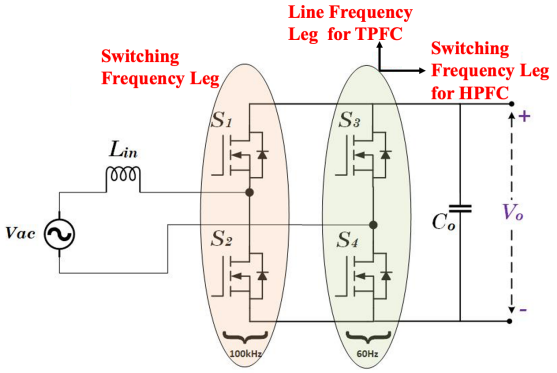

Fig. 2 Power circuit of the PFC converter: identical for TPFC and HPFC

Increasing the switching frequency markedly reduces the size of the converter's input filter. Nevertheless, when operating at a higher frequency, effectively managing the EMI noise emitted becomes essential, particularly in applications where the converter is directly connected to the grid. Adherence to the FCC Class A/B standards spanning from 150kHz to 30MHz is obligatory, necessitating rigorous EMI noise suppression measures. As the EMI filter is connected between the grid and the front end of the PFC converter, the three basic requirements that must be considered for designing DM EMI filters are as follows: (i) it should be able to suppress the EMI noise below standard level, (ii) it should not affect the power factor, and (iii) the system stability should not be impacted by the new zeros and poles introduced by the EMI filter transfer function [7]. The research done in [8] only discusses DM EMI noise for a traditional boost PFC converter functioning in critical conduction mode at various voltage and power levels. On the other hand, this paper explains about the DM EMI noise and the EMI filter design for a more advanced PFC topology such as

979-8-3503-0500-5/23/$31.00 ©2023 IEEE

TPFC and HPFC operating in continues conduction mode (CCM). In [9], the similar PFC topology as of [8] alongside its EMI compliance mechanism is discussed; however, the comprehensive design methodology while accounting for passives volume minimization and other converter constraints is absent in the discussion, which is described thoroughly in this paper. The works conducted in [10] and [11] provide extensive information on the architectures of EMI filter networks and the volumetric optimization of EMI filters in three-phase PFC converters, which can be consulted to gain a better understanding of these topics. The TPFC related analysis presented in this paper is carried out from the [7] and further the comparison between TPFC and HPFC is thoroughly explained in this paper. However, the impacts on the converter volume, efficiency, THD and system stability are disregarded in a gbroad-spectrum design of the DM EMI filter.

II. Mathematical Formulation of the Input Currrent Frequency Response for TPFC and HPFC Converters

An extensive comparison of the theoretically modeled duty formation and FFT analysis of the input current for the investigated PFC topologies are discussed in this section.

A. Mathematically Modeled the Duty Formation for TPFC and HPFC Converters

For the PFC converters, the input current can be expressed as the combination of the fundamental and the switching frequency ripple components as described in equation (1).

$$i_{in,actual} = I_{pk}\sin(\omega_g t) + i_{in,ripple} \quad (1)$$

where, $w_g = 2\pi f_g$ and f_g is the line frequency.

For TPFC and HPFC, the equation of ripple component over a switching cycle can be expressed as in equations (2) and (3).

$$i_{ripple,TP} = \begin{cases} \frac{V_{pk}\sin(wt)}{L}\cdot D\cdot T_s, & 0 < t < D\cdot T_s \\ \frac{V_o - V_{pk}\sin(wt)}{L}\cdot(1-D)\cdot T_s, & D\cdot T_s < t < T_s \end{cases} \quad (2)$$

$$i_{ripple,HB} = \begin{cases} \frac{V_O + V_{pk}\sin(wt)}{L}\cdot DT_s, & 0 < t < DT_s \\ \frac{V_o - V_{pk}\sin(wt)}{L}\cdot(1-D)T_s, & DT_s < t < T_s \end{cases} \quad (3)$$

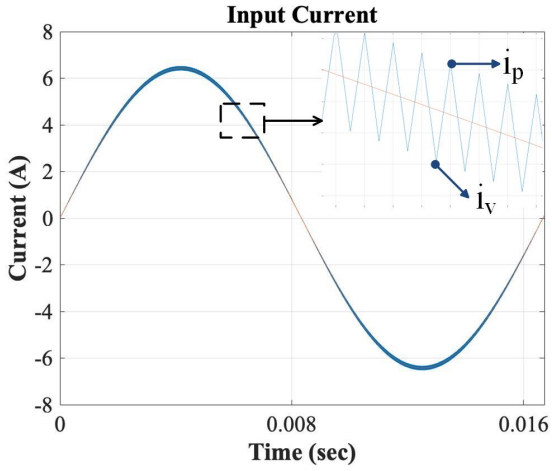

Fig. 3 Mathematically reconstructed input Current: TPFC

where, duty cycle and switching period are denoted by D and T_s.

The inner current loop controller function output determines the duty cycle, and the controller pushes to minimize the differential error when comparing the measured current with the current reference, produced by the outer loop voltage compensator, which accounts the component of the current at only fundamental frequency. Mathematically, the measured input current can be expressed as,

$$i_{in,actual} = \sum_{n=1,3,5,\ldots} a_n\cdot\sin(nw_g t) + b_n\cdot\cos(nw_g t) \quad (4)$$

As a duty cycle is derived from the controller, the most generalized equation for the duty cycle can be written as,

$$D(t) = K_p\left(I^*\sin(w_g\cdot t) - i_{in,actual}(t)\right) + K_i\int\left(I^*\sin(w_g\cdot t) - i_{in,actual}(t)\right) \quad (5)$$

where, K_p and K_i are the PI controller parameters and I^* is the transconductance reference generated from voltage loop compensator output.

The following expression establishes a relationship between the duty cycle and the current loop controller coefficients, which is essential for completing the frequency response characterization of the input currents. It is obtained by substituting the value of equation (4) into equation (5).

$$D = A_1\sin(w_g t + \emptyset_g) + \sum_{n=1,3,5,\ldots} A_n\sin(nw_g t + \emptyset_s) \quad (6)$$

where,

$$A_1 = \sqrt{(K_p\cdot I^*)^2 + \left(\frac{(K_i\cdot I^*)}{w_g}\right)^2}$$

$$\emptyset_g = \tan^{-1}\left(-\frac{K_i}{K_p\omega_g}\right)$$

$$A_n = \sqrt{\left(K_p a_n + \frac{K_i b_n}{w_s}\right)^2 + \left(K_p b_n + \frac{K_i a_n}{w_n}\right)^2}$$

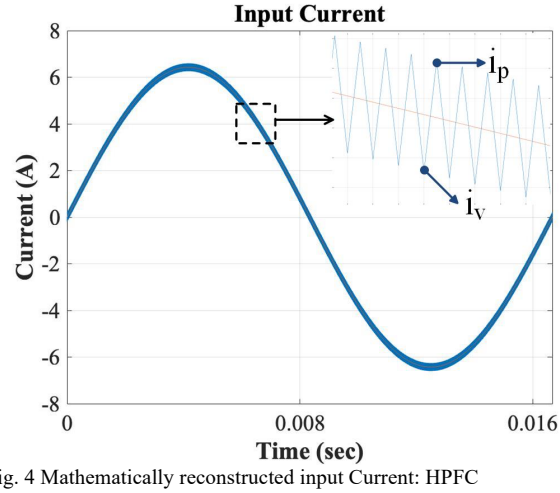

Fig. 4 Mathematically reconstructed input Current: HPFC

$$\emptyset_s = \tan^{-1}\left(\frac{\left(K_p b_n + \frac{K_i a_n}{w_s}\right)}{\left(K_p a_n + \frac{K_i b_n}{w_s}\right)}\right)$$

B. *Comparison of between the FFT-based mathematical model and simulation analysis for TPFC and HPFC converters*

The input current waveforms obtained through the mathematical formulations described previously are illustrated in Fig. 3 and Fig. 4. These figures correspond to the TPFC and HPFC configurations, respectively. In the switching ripples, i_p corresponds to the peak component and i_v corresponds to the valley component. From Fig. 3 and Fig. 4, it can be observed that the average of i_p and i_v forms the instantaneous value of the input current fundamental component and as shown in equation (7).

$$i_p(t) + i_v(t) = 2 \cdot I_{pk} \sin(w_g \cdot t) \quad (7)$$

where, the peak value of the input current can be written as $I_{pk} = \frac{2P}{V_{pk}}$ and P is the Power.

The mathematical formulations for the input current ripple falling edge of are identical for both the converters topologies, which can then be verified through the equations (3) and (4) and it can be expressed in terms of i_p and i_v as follows.

$$i_p(t) - i_v(t) = -\frac{V_o - V_{pk} \cdot sin(wt)}{L} \cdot (1 - D) \cdot T_s \quad (8)$$

Applying Fourier series on the mathematically reconstructed input current waveshape, the following can be formulated.

$$i_{in}(t) = \sum_{<n>}(a_n \sin(n \cdot w_g \cdot t) + b_n \cos(n \cdot w_g \cdot t)) \quad (9)$$

The instantaneous values of the a_n and b_n can be determined from the following equations (10) and (11).

$$a_n = \frac{2}{T}\int_0^T i_{in}(t)\, cos(n \cdot w_g \cdot t)\, dt \quad (10)$$

$$b_n = \frac{2}{T}\int_0^T i_{in}(t)\, sin(n \cdot w_g \cdot t)\, dt \quad (11)$$

For TPFC converter, the Fourier series coefficients are expressed in equations (12) and (13) and so for HPFC converter in equations (14) and (15).

$$a_n = \frac{2}{T}\sum_{n=0,1,2,\ldots}\left[\int_{nT_s}^{nT_s+DT_s}\left(i_v + \frac{V_{in}}{L}t\right) cos(n \cdot w_g \cdot t)\ dt + \int_{nT_s+DT_s}^{(n+1)T_s}\left(i_p - \frac{V_o - V_{in}}{L}t\right) cos(n \cdot w_g \cdot t)\ dt\right] \quad (12)$$

$$b_n = \frac{2}{T}\sum_{n=0,1,2,\ldots}\left[\int_{nT_s}^{nT_s+DT_s}\left(i_v + \frac{V_{in}}{L}t\right) sin(n \cdot w_g \cdot t)\ dt + \int_{nT_s+DT_s}^{(n+1)T_s}\left(i_p - \frac{V_o - V_{in}}{L}t\right) sin(n \cdot w_g \cdot t)\ dt\right] \quad (13)$$

$$a_n = \frac{2}{T}\sum_{n=0,1,2,\ldots}\left[\int_{nT_s}^{nT_s+DT_s}\left(i_v + \frac{V_o + V_{in}}{L}t\right) cos(n \cdot w_g \cdot t)\ dt + \int_{nT_s+DT_s}^{(n+1)T_s}\left(i_p - \frac{V_o - V_{in}}{L}t\right) cos(n \cdot w_g \cdot t)\ dt\right] \quad (14)$$

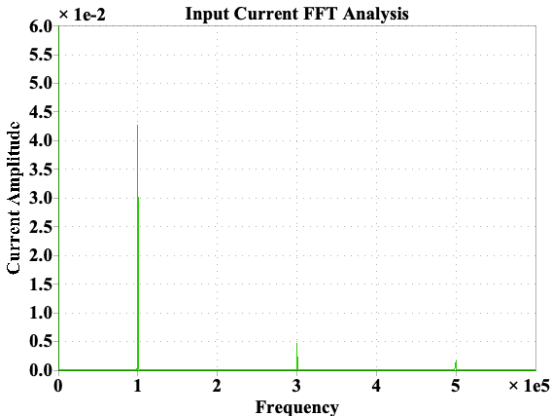

Fig. 5 Input Current Harmonics: Totem-pole PFC

$$b_n = \frac{2}{T}\sum_{n=0,1,2,\ldots}\left[\int_{nT_s}^{nT_s+DT_s}\left(i_v + \frac{V_o + V_{in}}{L}t\right) sin(n \cdot w_g \cdot t)\ dt + \int_{nT_s+DT_s}^{(n+1)T_s}\left(i_p - \frac{V_o - V_{in}}{L}t\right) sin(n \cdot w_g \cdot t)\ dt\right] \quad (15)$$

From the equations (12) to (15), the terms a_n and b_n are repeating over a cycle of every 60Hz. The equation (16) can be used to calculate the harmonic components of the input current at different multiples of the fundamental frequency.

$$< i_{in} >_n = \sqrt{(a_n^2 + b_n^2)} \quad (16)$$

In order to describe the harmonic components present in the input current at all the integer multiples of the fundamental frequency, FFT analyses of the mathematically reconstructed input current for TPFC and HPFC converters are shown in Fig. 5 and Fig. 6, respectively. In spite of having similar design parameters, it is clear from this analysis that the magnitudes of the switching harmonic components are larger in the HPFC than the TPFC. A greater current ripple in the HPFC input current, primarily due to higher voltage applied across the boost inductor and hence a greater charging slope for HPFC $\left(of\ \frac{V_{in}+V_o}{L}\right)$ compared to the TPFC $\left(of\ \frac{V_{in}}{L}\right)$ case. Furthermore, the input current in TPFC includes Zero-Crossing Distortion (ZCD) due to discontinuous duty cycle profile [7], while that is absent in HPFC, primarily due to a continuous time-variant and sinusoidal profile of the duty cycle. Based on this analysis, the

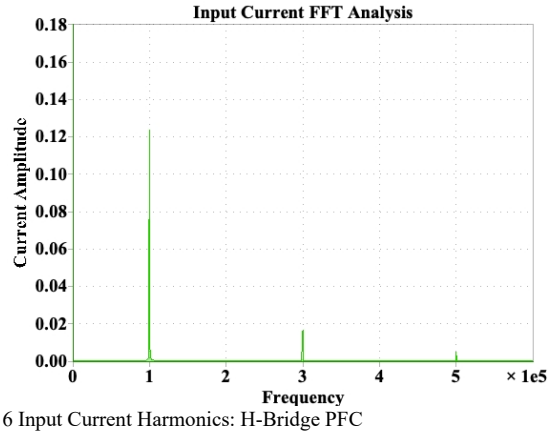

Fig. 6 Input Current Harmonics: H-Bridge PFC

TABLE I. COMPARATIVE INPUT CURRENT THD ANALYSIS: MATHEMATICAL MODEL VS. SIMULATION MODEL VS. HARDWARE EXPERIMENT FOR TOTEM-POLE PFC AND H-BRIDGE PFC CONVERTERS

Power	Model Type	PFC Converter Type	Input Voltage ($V_{IN,RMS}$)	Input Current ($I_{IN,RMS}$)	Power Factor	Output Voltage (V_{DC})	Total Harmonic Distortion (%)
500 W	Mathematical	Totem-pole	110 V	4.545 A	0.999	400 V	0.94 %
500 W	Mathematical	H-Bridge	110 V	4.545 A	0.999	400 V	2.39 %
500 W	Simulation	Totem-pole	110 V	4.545 A	0.989	400 V	1.47 %
500 W	Simulation	H-Bridge	110 V	4.545 A	0.999	400 V	2.86 %
500 W	Hardware Experiment	Totem-pole	110 V	4.896 A	0.983	400 V	1.91 %
500 W	Hardware Experiment	H-Bridge	110 V	4.546 A	0.989	400 V	3.47 %

input current in HPFC has average 1.45% higher THD compared to that of TPFC. The extensive comparison of the THD values of the input-current obtained through the analytical model, simulation model, and hardware experiments are tabulated in Table I for both the PFC topologies that indicate a close mutual agreement.

III. DESIGN METHODOLOGY OF DM EMI FILTER AND COMPARISON OF THE REQUIREMENT IN TPFC AND HPFC

This section illustrates a thorough optimization process conducted for the design of a multi-constraint DM EMI filter. This optimization takes into account the ideal specifications for both the PFCs, 110V 60Hz input voltage, and 500W rated power. Referring the FCC Class A standards subjected to EMI emission in EV charging, the objective function of design is to comply the EMI noise within the standard limits. In Figure 7, the configuration of a DM EMI filter is depicted, showcasing its essential components, including a DM filter inductor (LDM) and DM filter capacitors (CDM1 and CDM2). The DM noise comprises various switching harmonics, which originate from the ripple present in the input current. The DM EMI noise at the LISN may be formulated using the mathematical relationships listed below in (17),

$$EMI_{noise}(in\ dB\mu V) = 20\log\left(FFT(i_{in}(t)\cdot 50\cdot 10^{6}\right) \quad (17)$$

Through the Fast Fourier analysis based analytical model, the spectral characteristics of noise are determined. Fig. 8 and Fig. 9 illustrate the theoretically predicted EMI noise for the input currents of TPFC and HPFC, respectively. Notably, at the switching frequency (100kH) and its associated integral harmonics, the current peaks are perceptible.

An increased switching frequency results in elevated DM EMI noise emission, consequently necessitating more stringent attenuation measures. The requisite attenuation level is

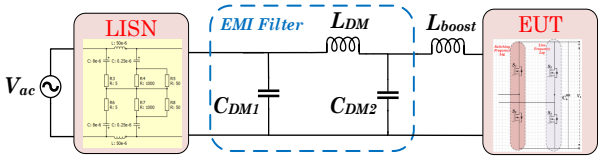

Fig.7 EMI noise measurement set-up and EMI Filter placement

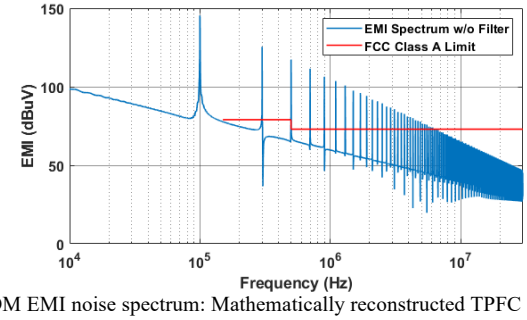

Fig. 8 DM EMI noise spectrum: Mathematically reconstructed TPFC

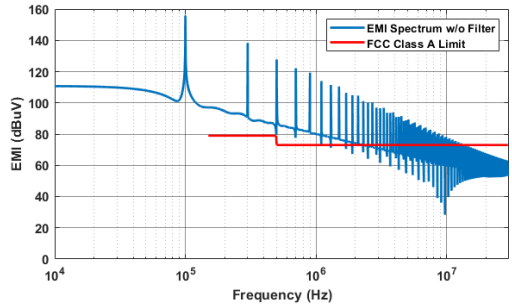

Fig. 9 DM EMI noise spectrum: Mathematically reconstructed HPFC

calculated by deducting the EMI noise spectrum from the specified limit of the FCC Class A EMI standard. To ensure dependable EMI performance of the PFC converters, a safety margin of approximately 6dB is maintained. Following the designated attenuation criteria and design frequency, a two-stage DM EMI filter is built to address amplified high-frequency noises and elevated-Q peaks in the spectrum, surpassing the defined EMI standard threshold. Applying the attenuation condition as a constraint, the modeling and volumetric optimization methodologies elucidated in [11] are utilized to ascertain the minimum LC product, formulated as follows.

$$Att_{req}(f_D) = (2\pi f_D)^4 (L_{DM} C_{DM1} L_{boost} C_{DM2}) \quad (18)$$

where, L_{boost} states the boost inductor

The first peak, which surpasses the FCC Class A standard threshold by 54dB and is located at 300kHz for the TPFC design, can be seen when examining the noise in the absence of an EMI filter as inferred from the theoretical model. Consequently, the parameters of the DM EMI filters are calculated and employed: L_{Boost}=500□H, L_{DM}=100□H, and C_{DM1}=C_{DM2}=10nF.

TABLE II. HARDWARE IMPLEMENTATION DESIGN SPECIFICATIONS: TOTEM-POLE PFC AND H-BRIDGE PFC

Parameters	Specifications
Input Voltage (V_{in})	110 V_{RMS}, 60 Hz, 1Ø
Rated Power (P_{out})	500 Watt
Output Voltage (V_{out})	400 V_{DC}
Boost Inductor (L_{in})	500 □H
Output Capacitor (C_{out})	2 mF
Switching Frequency (f_{sw})	100 kHz

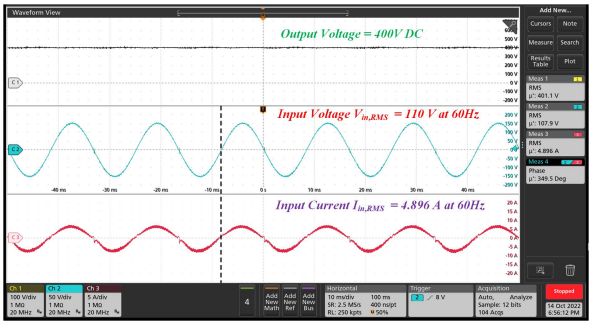

Fig. 10: Experimental Results of TPFC at Rated 500W Load Power for (i) Output Voltage (V_{out}), (ii) Input Voltage (V_{in}), and (iii) Input Current (I_{in})

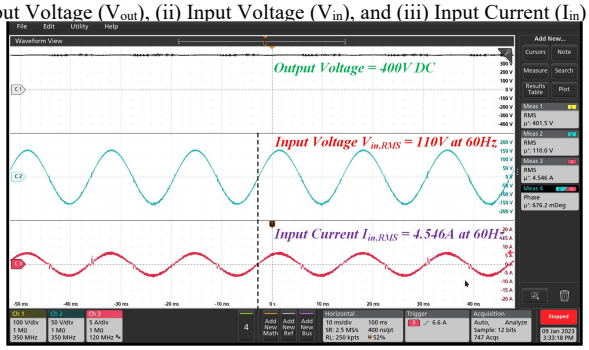

Fig. 11: Experimental Results of HPFC at Rated 500W Load Power for (i) Output Voltage (V_{out}), (ii) Input Voltage (V_{in}), and (iii) Input Current (I_{in})

IV. INVENSTIGATION OF THE EXPERIMENTAL RESULTS

A proof-of-concept 500W converter is designed, fabricated, and evaluated in order to confirm the efficient functioning of both PFC converters. Both the converters are operated at a switching frequency of 100kHz. The steady state experimental results illustrated in Fig. 10 and Fig. 11 refer to the TPFC and HPFC, respectively. Besides of near-unity power factor and steady output voltage regulations, the TPFC power factor is measured

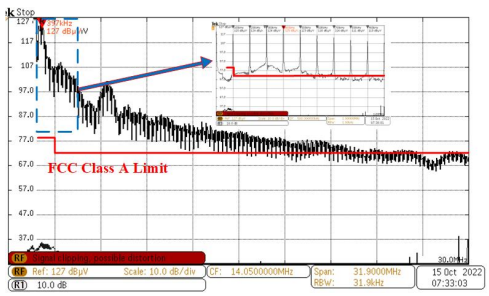

Fig. 12 The EMI spectrum of the input current without incorporating EMI Filter in TPFC.

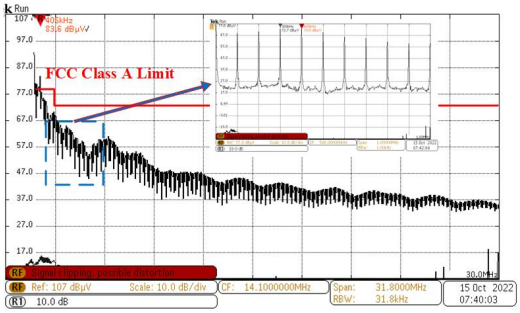

Fig. 13 The EMI spectrum of the input current with EMI filter in TPFC.

to be 0.983, while the HPFC attains an improved power factor of 0.989, mainly due to the mitigation of zero crossing distortion.

In Fig. 12, the input current EMI spectrum for TPFC without the EMI filter is shown. When the resulting spectrum is compared to the FCC class A EMI standard, it is evident that the input current spectrum exceeds the established standard limit at several frequencies. In order to mitigate and adhere to the necessary EMI noise standards, a DM EMI filter is employed, with its element values derived from the previously established mathematical model at the input stage of the converter. The filter parameters employed in the network for implementation are as follows: L_{DM}=100□H and C_{DM1}= C_{DM2}=10nF.

Fig. 13 illustrates an attenuated EMI spectrum by 50dB at 300kHz, which adheres to the FCC Class A standard throughout the frequency range of 150kHz to 30MHz. The area that has been zoomed in exposes the input current switching harmonic peaks up to 1 MHz, which remain much below the standard limit. The input current EMI spectrum for HPFC is similarly displayed in Fig. 14 without implementing an EMI filter. The DM EMI noise generated by the HPFC converter is higher than that of the TPFC, as was stated in Section III, and the corresponding EMI test carried out on the hardware prototype indicates that the HPFC requires 60dB attenuation at 200kHz. In the HPFC hardware prototype, first, implementing the DM EMI filter designed for TPFC specifically in order to investigate the suppression of DM EMI noise emission, as depicted in Fig. 15. Although the noise emission requirements are met by the EMI filter with TPFC, the HPFC requires an additional 24dB suppression at 200kHz from the EMI filter. The completely compliant EMI spectrum for HPFC can be seen in Fig. 16 after the EMI filter was extended using DM capacitors of 15nF instead of 10nF to attenuate the excess noise of 24dB.

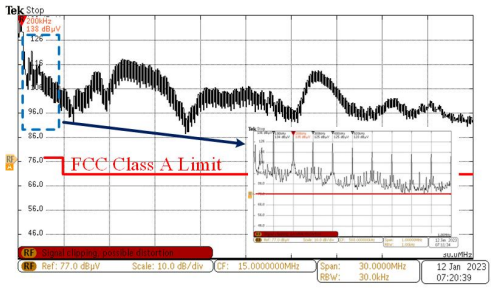

Fig. 14 The EMI spectrum of the input current without incorporating EMI filter in HPFC.

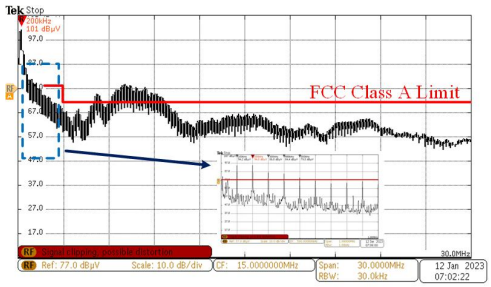

Fig. 15 The EMI spectrum of the input current when incorporating the EMI filter tailored for TPFC into HPFC.

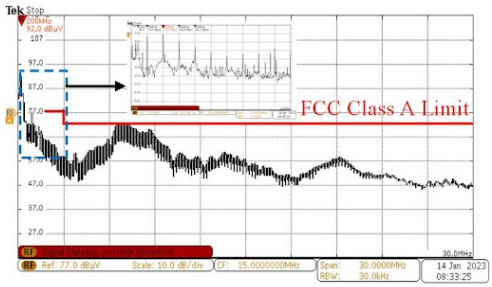

Fig. 16 The EMI spectrum of the input current when incorporating the EMI filter extensively designed for HPFC.

V. Summary of Experimental Findings

A. Efficiency

Both the converters operate with high efficiency which is evident from the experimental results. Performing an experiment on the rated 500 W prototypes of both converters, the efficiency achieved for the TPFC is 98.45% and for HPFC converter is 97.86%. The HPFC comprises of higher switching loss compared to TPFC for the identical test conditions due more no. of switched operating at high switching frequency.

B. Total Harmonic Distortion (THD)

In the HPFC, the switching ripples over the fundamental sine wave are approximately 80% higher than that of TPFC. As observed from the mathematical model of HPFC, the current ripple magnitude near the zero crossing is approximately 24% greater than the TPFC primarily due to higher charging/discharging slope of the inductor current for an identical boost inductance value, as evident from Table I.

C. EMI Filter requirement

When compared to TPFC, HPFC has more high switching frequency components and their harmonic amplitudes, which causes the switching circuit to emit more EMI noise. The converter does not comply with the attenuation requirement and an additional 24dB of attenuation at 200kHz is needed when the EMI filter designed for TPFC is used in HPFC. The DM filter capacitor values are increased by 50% for HPFC converters in order to achieve the needed attenuation, resulting in a 20% larger volume EMI filter than for TPFC converters.

VI. Conclusions

This paper presents a comprehensive comparison of the TPFC and HPFC converter. Over the duration of a complete line cycle and taking into account duty cycle change, a comprehensive mathematical model of the input current characteristic is developed. A comparison is made between the input current THDs for the two PFC topologies using a mathematical model, a simulation model, and hardware experiments. The paper also describes how to construct EMI filters that reduce EMI noise and satisfy FCC class-A EMI standard requirements. A 500W hardware prototype is created to verify the performance of both PFC topologies. According to the experimental findings, the input power factor for TPFC and HPFC converters, respectively, was 0.983 and 0.989 at the rated load condition, while their efficiencies are 98.45% and 97.86%. The EMI filters are developed for both of the PFC converters by using mathematical models of the input current frequency response. For ensuring compliance with the FCC class A standard, it was discovered that the EMI filter designed for HPFC converters had a 20% larger volume than that of TPFC converters.

References

[1] A. Kazemtarghi, A. Chandwani, N. Ishraq and A. Mallik, "Active Compensation-based Harmonic Reduction Technique to Mitigate Power Quality Impacts of EV Charging Systems," in IEEE Transactions on Transportation Electrification, 2022, doi: 10.1109/TTE.2022.3183478.

[2] A. H. Dabbagh, H. Arvani, H. Gholizadeh and E. Afjei, "A SiC-Based Hybrid PFC-Inverter for On-board EV Chargers," 2022 13th Power Electronics, Drive Systems, and Technologies Conference (PEDSTC), Tehran, Iran, Islamic Republic of, 2022, pp. 380-385, doi: 10.1109/PEDSTC53976.2022.9767296.

[3] I. Alzuguren, A. Garcia-Bediaga, A. Avila, A. Rujas and M. Vasic, "Single-Phase Single-Stage PFC Based on a Novel Floating Capacitor Filter for Electric Vehicle On-Board Charger Application," 2022 IEEE Energy Conversion Congress and Exposition (ECCE), Detroit, MI, USA, 2022, pp. 1-7, doi: 10.1109/ECCE50734.2022.9947698.

[4] A. Dixit, K. Pande, S. Gangavarapu and A. K. Rathore, "DCM-Based Bridgeless PFC Converter for EV Charging Application," in IEEE Journal of Emerging and Selected Topics in Industrial Electronics, vol. 1, no. 1, pp. 57-66, July 2020, doi: 10.1109/JESTIE.2020.2999595.

[5] A. Chandwani, S. Dey and A. Mallik, "Parameter-Variation-Tolerant Robust Current Sensorless Control of a Single-Phase Boost PFC," in IEEE Journal of Emerging and Selected Topics in Industrial Electronics, vol. 3, no. 4, pp. 933-945, Oct. 2022, doi: 10.1109/JESTIE.2021.3128809.

[6] J. P. M. Figueiredo, F. L. Tofoli and B. L. A. Silva, "A review of single-phase PFC topologies based on the boost converter," 2010 9th IEEE/IAS International Conference on Industry Applications - INDUSCON 2010, Sao Paulo, Brazil, 2010, pp. 1-6, doi: 10.1109/INDUSCON.2010.5740015.

[7] P. Rathod, N. Ishraq, A. Chandwani and A. Mallik, "Comprehensive Mathematical Modelling and Design of DM EMI Filter for Totem-pole PFC Converter," 2022 IEEE 1st Industrial Electronics Society Annual On-Line Conference (ONCON), kharagpur, India, 2022, pp. 1-6, doi: 10.1109/ONCON56984.2022.10126532.

[8] F. Yang, X. Ruan, Q. Ji and Z. Ye, "Input Differential-Mode EMI of CRM Boost PFC Converter," in IEEE Transactions on Power Electronics, vol. 28, no. 3, pp. 1177-1188, March 2013, doi: 10.1109/TPEL.2012.2206612.

[9] J. Zhang, J. Shao, P. Xu, F. C. Lee and M. M. Jovanovic, "Evaluation of input current in the critical mode boost PFC converter for distributed power systems," APEC 2001. Sixteenth Annual IEEE Applied Power Electronics Conference and Exposition (Cat. No.01CH37181), Anaheim, CA, USA, 2001, pp. 130-136 vol.1, doi: 10.1109/APEC.2001.911638.

[10] Dey, S.; Mallik, A. "A Comprehensive Review of EMI Filter Network Architectures: Synthesis, Optimization and Comparison" in Electronics 2021, 10, 1919.

[11] S. Dey, A. Mallik and S. Mishra, "A Mathematical Design Approach to Volumetric Optimization of EMI Filter and Modeling of CM Noise Sources in a Three-Phase PFC," in IEEE Transactions on Power Electronics, vol. 37, no. 1, pp. 462-472, Jan. 2022, doi: 10.1109/TPEL.2021.3097963.